ACS APPLIED NANO MATERIALS

www.acsanm.org Article

# Role of the Deposition Distance on Nanorod Growth and Flux Pinning in $BaZrO_3$-Doped $YBa_2Cu_3O_{6+x}$ Thin Films: Implications for Superconducting Tapes

Moe Moe Aye,* Elmeri Rivasto,* Hannes Rijckaert, Sari Granroth, Heikki Palonen, Hannu Huhtinen, Isabel Van Driessche, and Petriina Paturi

Cite This: *ACS Appl. Nano Mater.* 2022, 5, 18159−18167 Read Online

ACCESS | Metrics & More | Article Recommendations | Supporting Information

**ABSTRACT:** A complex deposition process of high-temperature superconducting (HTS) thin films and coated conductors is usually optimized by concentrating on the crystalline quality of the material, thus getting the best possible critical temperature and self-field properties. However, most of the HTS power applications that are based on coated conductors act at high magnetic fields, and thus an alternative approach focusing on the formation of an optimal network of columnar flux pinning centers is more reasonable. Therefore, we systematically show how a lengthening of the deposition distance produces perfectly aligned and distinctly longer self-assembled $BaZrO_3$ (BZO) nanorods within the $YBa_2Cu_3O_{6+x}$ (YBCO) matrix. This method unambiguously enhances in-field properties such as pinning force, critical current density, and its isotropy along the YBCO *c* axis. The experimental results, especially formation of the *c* peak where the relative length of the nanorod is a key issue, are confirmed by the vortex dynamics simulations. Finally, we present a semiquantitative model governing the formation of nanorods that explains the experimentally observed improved nanorod growth as a function of the deposition distance via the associated variation of the fractional partial pressure between atomic species within the laser plume.

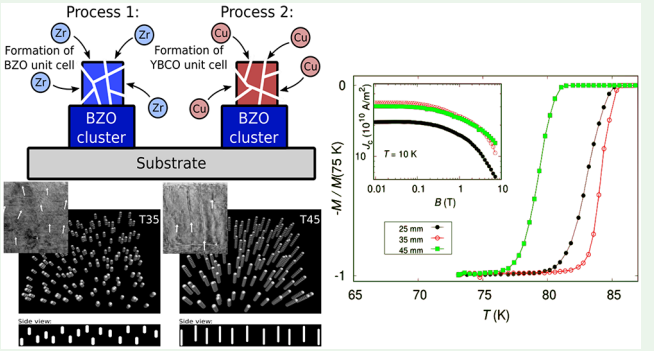


**KEYWORDS:** *high-temperature superconductivity, pulsed-laser deposition, artificial pinning centers, flux pinning, coated conductors*



## INTRODUCTION

Pulsed-laser deposition (PLD) is a thin-film growth technique in which the laser−target interaction, formation of laser plasma, and its shock-wave propagation together with the film growth mechanism form a very complex physical phenomenon.[1] The versatility of the method in growing films of almost any kinds of compounds makes PLD one of the most powerful techniques in high-temperature superconducting (HTS) thin-film and coated conductor technologies, which again are used as basic construction units in most of HTS electric power applications.[2,3] Especially, PLD has the capability of reproducing the source composition of even multielemental compounds such as $YBa_2Cu_3O_{6+x}$ (YBCO) when the deposition conditions and thus the system growth parameters are optimized. Furthermore, when the YBCO target is doped with artificially produced and self-assembled pinning centers (APCs), the structure of APC depends on the material and growth temperature. A columnar APC structure is observed in a high lattice mismatch (LM) system such as $BaZrO_3$ (BZO)/YBCO (9%) but not in systems where LM is lower, as with $Y_2O_3$ nanoparticles (2.5%).[4] Growth kinetics have been observed to play a crucial role in controlling the length and splay of columns of the nanorods within the YBCO matrix.[5−7] In nanorods such as BZO, the BZO volume concentration calculated from the dimensions of the nanocolumns formed in the resulting YBCO/BZO film has been concluded to be considerably higher, even more than 5-fold, than that in the original target.[8−10]

The crystallographic goodness of the YBCO film is not the only major factor, although it clearly has the most important relevance for the self-field critical current density $J_c(0)$.[11,12] Also, the superconducting properties at high fields together with the maximal flux pinning properties need to be optimized[11,13,14] especially when fulfilling the requirements in future coated conductor and HTS electrical power application technologies. Because, during the deposition process, the target−substrate distance is very critical for getting the correct

Received: September 14, 2022
Accepted: November 14, 2022
Published: November 25, 2022

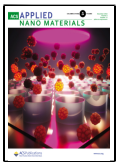

stoichiometry on the surface of the substrate, we have to perform a balancing act between two issues: on the one hand, the distance where YBCO grows crystallographically must be as perfect as possible, and, on the other hand, the BZO nanorods, which are solid and continuous along the out-of-plane direction of the YBCO matrix, need to be optimized. Especially, during propagation of the laser plume, the plasma emission and its interaction with the background gas affect the stoichiometry of the ejected flux as well as the particulate formation and their coalescence when the deposition distance is increased.[15,16] The deposition distance is also strongly related to the oxygen pressure during the deposition because the collisions between the plume particles and the background gas are influenced by the specific heats of the elements, thus forming a critical distance above which the proportion of smaller particles decreases and larger particulates start to appear.[17−19]

The effect of the deposition distance and laser frequency in the PLD process on the growth of undoped YBCO films has been previously studied.[20,21] Increasing laser frequency was observed to promote the formation of dislocations within the YBCO matrix, and thus the optimal frequency turned out to be field-dependent.[21] The general optimization of the laser frequency for more complex systems, such as doped YBCO, is considered to be rather difficult to address because of the complex and difficult-to-predict effects of laser−target interaction and growth dynamics on the substrate. On the contrary, the deposition distance is far more easy to optimize because it can be considered somewhat independent of the other deposition parameters. In addition, the effect of the deposition distance can be addressed with simple plume propagation and film growth models as done in ref 20, where the deposition distance was observed to have a clear optimum value with respect to the superconducting properties of the resulting undoped YBCO film in the wide field range. However, the effect of the deposition distance has not yet been systematically studied in the presence on self-assembled dopants, such as BZO. The deposition distance, in particular, can be considered to have a significant effect on the assembly of the nanorod structures due to the expected variation of partial pressures associated with different atomic species within the plume. In this work, we study how the deposition distance affects the nanorod assembly in the BZO-doped YBCO film. The effect of the obtained APC nanorod structure on the superconducting properties is magnetically and resistively investigated, and the results are compared with the molecular dynamics (MD) simulations to better understand the role of size, shape, and number of APCs on the angular-dependent critical current density. Furthermore, we present a quantitative model that explains the experimentally observed differences in the nanorod assembly within films deposited at different distances from the target.

## EXPERIMENTAL DETAILS

The 4 wt % BZO-doped YBCO targets were manufactured by the standard solid-state method using a final sintering temperature of 920 °C.[13,22] The thin films were prepared by PLD on (100) $SrTiO_3$ (STO) substrates using a 308 nm XeCl excimer laser and varying a distance between the target and substrate in the range of 25−45 mm. All of the other PLD parameters such as the deposition rate, deposition temperature, and oxygen pressure were fixed during the deposition. The details of the PLD system and the deposition parameters have been given elsewhere.[23]

The crystallographic properties, including formation of the YBCO and BZO phases, were determined by X-ray diffraction (XRD) measurements with a PANalytical Empyrean diffractometer in the Bragg−Brentano mode. With the thin films, the incident X-ray beam was collimated with a Bragg−Brentano mirror using a $^1/_4°$ divergence slit and 0.04 rad Soller. With the target, a 0.3 × 1.3 mm microbeam collimator was used with the mirror. A PIXcel was used as a detector. The thicknesses of the films were measured by X-ray reflectivity (XRR). The surface morphology and elemental composition of the target as well as thin films were examined by scanning electron microscopy (SEM; FEI Apreo S field-emission scanning electron microscope with Schottky-type electron gun from Thermo Fisher Scientific) and energy-dispersive spectroscopy (EDS; Ultim Max Large Area SDD, Oxford Instruments). The EDS elemental maps were taken with a 10 kV acceleration voltage and a 0.80 nA beam current. Formation of the BZO nanorods was investigated by bright-field scanning transmission electron microscopy (BF-STEM; JEOL JEM 2200FS) using a 200 kV operating voltage. The samples for BF-STEM were prepared by cutting a cross-sectional lamella via the focused-ion-beam technique in a FEI Nova 600 Nanolab dual-beam scanning electron microscope using the *in situ* lift-out procedure with an Omniprobe extraction needle.[24]

The magnetic measurements were carried out with a Quantum Design Physical Property Measurement System (PPMS) system, where the onset critical temperatures, $T_c$, were determined from the alternating-current (ac) magnetization curves. The magnetic field dependences of the critical current densities, $J_c(B)$, at 10 K were determined from the opening of the hysteresis loops using the Bean model for rectangular films.[25] The angular-dependent transport properties were measured using a horizontal rotation option of the PPMS. The measurements were made in various magnetic fields at a temperature of 40 K with a 0−360° angular range using 3° steps. The measurement temperature of 40 K was chosen to be far enough from $T_c$ but still meeting the temperature requirements for technological applications.[13,26] The angular-dependent critical current densities around the *c*-axis peak were modeled by MD simulations.[27,28]

## RESULTS AND DISCUSSION

**Propagation of the Laser Plume.** Figure 1 shows a schematic illustration of how the visible laser plume propagates

| Distance (mm) | Zr/Y (%) | Zr/Cu (%) |
|---|---|---|
| 25 | 4.8 | 1.6 |
| 35 | 4.6 | 1.6 |
| 45 | 3.9 | 1.2 |

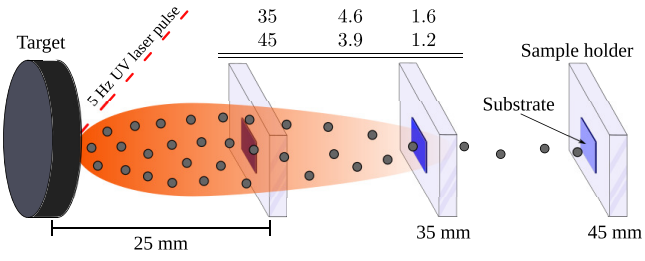


**Figure 1.** Elemental ratios of Zr/Y and Zr/Cu calculated from the quantitative elemental analysis of 4 wt % BZO-doped YBCO films deposited at different target−substrate distances (table). The figure shows a schematic illustration of how the visible laser plume is propagated in proportion to the substrate distance from the target.

in proportion to the substrate distance from the target. In an earlier optimization,[15,16] the zero-field superconducting properties of the undoped YBCO films are the best when the tip of the visible plume is close to the substrate surface, around 35 mm in our PLD system. To investigate the formation of BZO and its presence in the formed nanorods at different target−substrate distances, we investigated the elemental ratios of Zr/Y and Zr/Cu calculated from the quantitative elemental


https://doi.org/10.1021/acsanm.2c04054
ACS Appl. Nano Mater. 2022, 5, 18159−18167

analysis of BZO-doped YBCO films. On this basis, we can obtain from the table of Figure 1 that the number of Zr atoms in comparison with Y and Cu atoms in the plume seems to be constant up to the distance of 35 mm, above which the ratios of Zr/Y and Zr/Cu start to decrease slightly. This could give an assumption that the BZO/YBCO ratio is moderately decreased in the plume at the highest deposition distance. However, we do not expect a significant difference of the nominal contents in the formation of the YBCO and BZO ratio at various deposition distances, and the differences in the superconducting properties are more dependent on the deposition rate and related growth mechanisms.

**Growth of BZO within the YBCO Lattice.** The crystalline quality of the films was characterized by XRD, and the most important results are collected in the inset table of Figure 2 and also in the Supporting Information (SI). As can be seen in Table S1, the out-of-plane lattice parameter $c$ is slightly lengthened from the nominal value of 11.68 Å, clearly most at the longest deposition distance of T45. In addition, the $2\theta$ peaks as well as the rocking curve in the $\omega$ direction are the broadest in T45, indicating evident variation in the unit cells and shortened coherence ($r_c$) along the out-of-plane direction. Because the intensity ratio $I(005)/I(004)$ (Table S1) is well below 20 for all of the samples, we can conclude that the oxygen concentration is on the optimal level.[29]

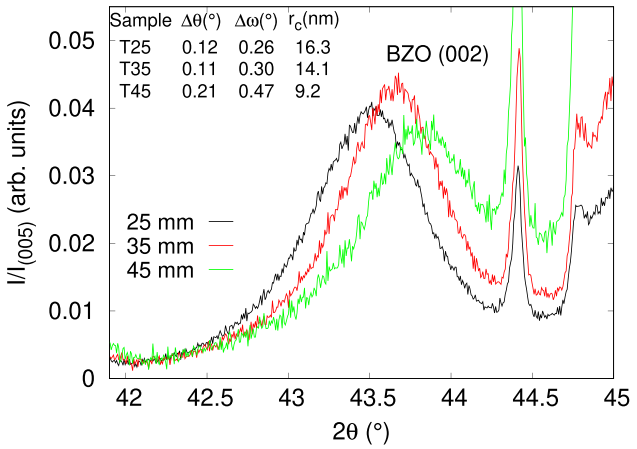


**Figure 2.** Relative XRD intensity ratios of the BZO (002) and YBCO (005) peaks that give BZO concentrations of 1.96, 2.00, and 2.03 wt % for YBCO films deposited at different target−substrate distances of 25, 35, and 45 mm, respectively.

The thicknesses of the films were extrapolated from the thickness of the thinnest 45 mm film, which was measured with XRR to be 122 nm. The extrapolation was done by scaling the thicknesses with the YBCO XRD peak intensities after correcting for the increasing absorption with increasing thickness. The obtained thicknesses of 122, 200, and 365 nm for the 45, 35, and 25 mm target-to-substrate distances, respectively, are in good agreement with the average thicknesses seen in the transmission electron microscopy (TEM) images (see below). The BZO concentrations of the films were calculated by comparing the theoretical intensity ratio of the BZO (002) and YBCO (005) peaks with the ratio of the corresponding observed intensities (Figure 2). The theoretical intensities were corrected using single-crystal Lorentz, polarization, absorption, and Debye−Waller factors.[30] On the basis of the XRD results, the obtained actual concentration of crystallized BZO is 2.0 wt % for all of the films. Interestingly, the mosaicities of both the YBCO and BZO phases, calculated from their rocking curves, decrease with decreasing target-to-substrate distance, which is in contrast with what one would expect when a film relaxes through defect formation with increasing thickness. This opposite behavior can be explained by decreasing surface mobility with increasing distance, which promotes more defect formation during the growth process and thus affects the number of vortex pinning centers in the film.

The microstructure of the BZO-doped YBCO films deposited at different distances was characterized by STEM, and the collection of cross-sectional BF-STEM images is presented in Figure 3. Contrary to our previous optimizations, where hardly any parameters effect the size of the nanorod, especially the nanorod diameter,[13,14,31] the deposition distance seems to have a great impact on the diameter and the tilting angle of the nanorod, as can be seen in Figure 3 and Table 1. In conclusion, the average diameter of the nanorod in the T25 film is about 8.6 nm, while in the film deposited at the longest distance of T45, it is only 4.6 nm, being reduced almost by half. The average length of the nanorod stays almost constant up to the distance of 35 mm, above which the rods lengthen distinctly.

The most dramatic change can be observed in the growth direction of the nanorod, where with the shortest deposition distance T25, the average tilting angle is almost 40° from the direction of the YBCO $c$ axis. As can be seen in Figure 3c, in a film of the longest deposition distance of T45, the nanorods are markedly oriented in the out-of-plane direction, clearly producing the most optimal flux pinning network in the film within the studied deposition distance range. However, even in

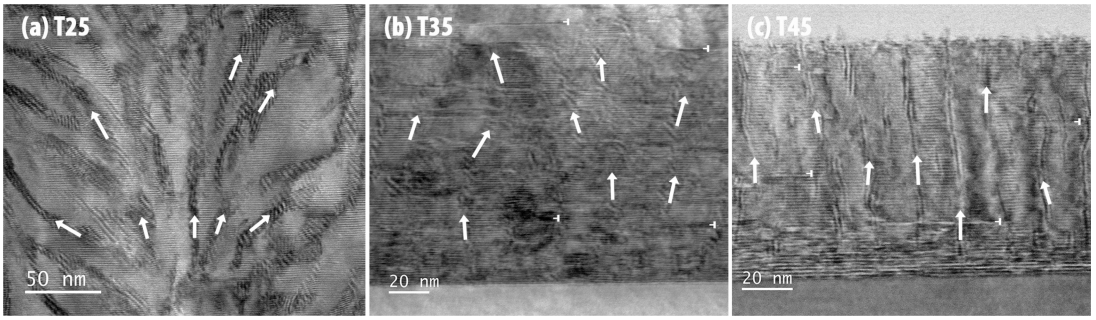


**Figure 3.** Cross-sectional BF-STEM images of the YBCO films deposited from the 4 wt % BZO-doped YBCO targets at different target−substrate distances of 25, 35, and 45 mm. The white arrows indicate the BZO nanorods.



https://doi.org/10.1021/acsanm.2c04054
ACS Appl. Nano Mater. 2022, 5, 18159−18167

**Table 1. Collection of the Obtained BF-STEM Results for BZO-Doped YBCO Films Grown at Different Deposition Distances**[a]

| sample | thickness (nm) | diameter (nm) | length (nm) | splay (deg) | nanorod density of YBCO/BZO (%) |
|---|---|---|---|---|---|
| T25 | 395 ± 5 | 8.6 ± 3.6 | 52.7 ± 15.1 | 36.9 ± 20.6 | 45.6/54.4 |
| T35 | 210 ± 5 | 5.9 ± 1.0 | 57.8 ± 14.1 | 9.1 ± 3.7 | 54.0/46.0 |
| T45 | 94 ± 5 | 4.6 ± 0.6 | 76.1 ± 5.1 | 7.1 ± 5.6 | 67.5/32.5 |

[a]The parameters are the film thickness as well as the BZO nanocolumn diameter and length, the average tilting angle in relation to the YBCO *c* axis, and the volume percentages between the YBCO and BZO nanorods.

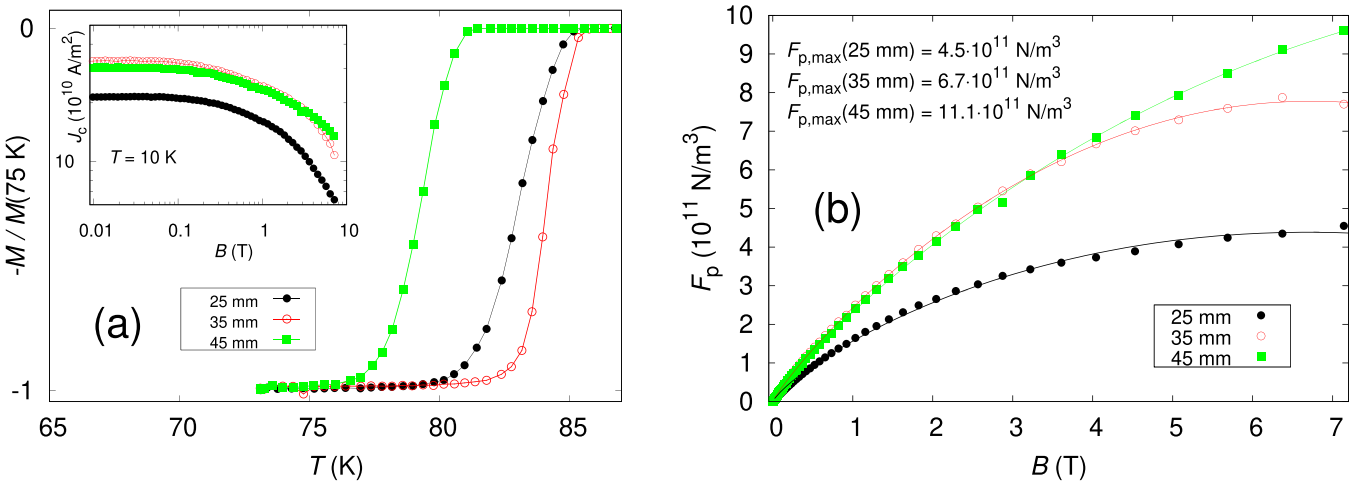


**Figure 4.** (a) Normalized ac magnetization as a function of the temperature and magnetic field dependencies of $J_c$ determined from the hysteresis loops at 10 K (inset) for BZO-doped YBCO films deposited at different target−substrate distances. (b) Pinning force $F_p$ values as a function of $B$. The curves are fits to eq 1, producing the maximum pinning forces for the BZO-doped YBCO films deposited at different distances, as collected in table form in the figure.

this film, a distorted area of thickness ≈ 20 nm next to the interface can be observed, and thus well-aligned nanorods start to grow above this. When looking at the volumetric ratio between the YBCO matrix and BZO nanorods in Table 1, it is obvious that the nanorod density decreased with increasing deposition distance from above 50% at T25 to 32.5% at T45. Because we have earlier demonstrated by XRD that the amount of crystallized BZO is independent of the deposition distance of ≈2% but, on the other hand, the relative Zr ratio measured by EDS is only slightly decreased with increasing deposition distance, being close to the nominal 4% value (Figure 1), the difference between the BZO content and nanorod density is more likely related to the composition of the nanorods, where distorted YBCO is also composed in the nanocolumns.[32−34]

**Deposition-Distance-Dependent Superconducting Properties.** As can be seen in the main panel of Figure 4a, the magnetically measured onset $T_c$ is the highest at ≈86 K and the transition is the sharpest in the T35 film, as was also optimized earlier when the most important criterion of the YBCO film was crystallographically as good as possible.[23] The critical temperature is slightly decreased in the T25 film, but $T_c$ is clearly diminished in the T45 film. The similar decreasing trend in $T_c$ with increasing deposition distance can be observed in resistivity measurements of the same samples, albeit the $T_c$ level is clearly higher because the current can find an optimal path through the YBCO matrix.

Degradation of the superconducting properties under the low-field range as a function of the deposition distance was previously observed for undoped YBCO films,[20] where the authors comprehensively discussed this effect by considering various plume propagation and film growth models. The degraded superconducting properties are evidently a result of the poorer crystalline quality of the films deposited at longer distances, which was ultimately explained by decreased kinetic energies of the atomic species arriving at the substrate. At lower kinetic energies, the reaction time of the adatoms on the substrate is increased, resulting in distorted nonuniform film growth. We want to further point out that the observed degradation of $T_c$ for the T45 film is not related to variation of the oxygen concentration within the YBCO lattice, as shown in Table S1.

When looking at the shapes of the $J_c(B)$ curves in the inset of Figure 4a, one can obtain a clear similarity in the T25 and T35 samples, although the level of $J_c$ in T35 is roughly 50% higher in the whole magnetic field range up to 8 T. Instead of this, the $J_c(B)$ curve of T45 follows approximately but slightly below the $J_c(B)$ curve of T35, but a clear crossover in the curves can be seen around the magnetic field of 3 T. This is in line with the remarkably higher pinning force values above 3 T determined by the formula $F_p(B) = BJ_c(B)$, as shown in Figure 4b. The maximum pinning force values $F_{p,max}$ shown in Figure 4b were calculated by fitting the $F_p$ data to the function[35−37]

$$\frac{F_p(B)}{F_{p,max}} = \frac{(p+q)^{p-1}p^q}{q^q}\left(\frac{B}{B_{max}}\right)^p\left(\frac{p+q}{p} - \frac{B}{B_{max}}\right)^q \quad (1)$$

where $p$, $B_{max}$, and $F_{p,max}$ are kept as free fitting parameters and $q$ is fixed to 1.1, as obtained earlier for BZO-doped YBCO.[37] The increased flux pinning properties such as $F_{p,max}$ and $J_c(B)$ at high fields in the T45 film can be explained by the relatively straight and lengthened BZO nanorods with optimal nanorod


https://doi.org/10.1021/acsanm.2c04054
ACS Appl. Nano Mater. 2022, 5, 18159−18167

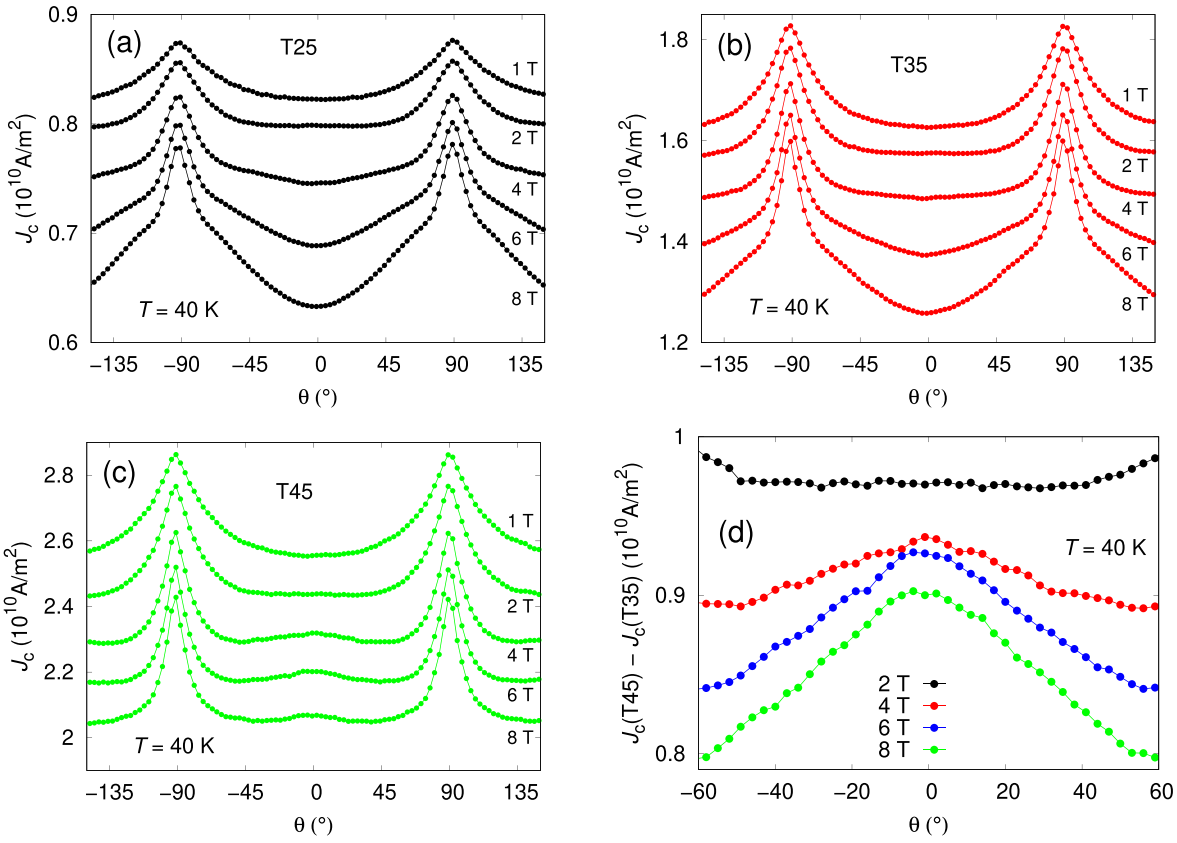


**Figure 5.** Angular-dependent $J_c(\theta)$ curves measured at 40 K and in various magnetic fields from 1 to 8 T for samples T25 (a), T35 (b), and T45 (c). The angle value $\theta = 0°$ corresponds to the YBCO *c* axis, and the values $\theta = -90°$ and $+90°$ correspond to the *ab* plane. (d) Relative difference in the *c*-axis peak of the $J_c(\theta)$ curves measured between samples T45 and T35 at 40 K and in different magnetic fields.

diameter that maximally pin the vortices along the YBCO *c* axis.[13,14,38,39]

The angular-dependent $J_c(\theta)$ curves measured at different magnetic fields for samples T25, T35, and T45 are collected in Figure 5. When comparing the results in films deposited at different distances, we can see that the absolute $J_c$ value through the whole angular range dramatically increased with increasing deposition distance, being more than 3 times greater in T45 than in T25. This means that the change in the growth mechanism, where particularly slow growth leads to a relatively thin final film, seems to produce superior flux pinning properties. Although the absolute $J_c$ is increased, the shape of the curves between T25 and T35 are almost identical. In sample T45, the shape of the *ab* peak remains the same as that in T35, but along the YBCO *c* axis at 0°, a peak starts to form at 4 T, especially when compared with the samples T25 and T35, where a relatively clear dip is visible along the YBCO *c* axis. This is fully in line with the structural properties shown earlier, where the nanorod alignment is greatly improved at the highest deposition distance of 45 mm. Similar behavior has also been observed in HTS films irradiated by heavy ions, where the defects parallel to the *c* axis produce a sharp and relatively narrow *c*-axis peak in $J_c(\theta)$ and the direction-dispersed defects clearly broaden and lower the formed *c*-axis peak of $J_c(\theta)$.[40−42] Therefore, we have shown here that, although the optimal deposition distance for crystallographically perfect YBCO is shorter, the improved flux pinning properties can be obtained when the target−substrate distance and thus the effective laser plume are longer. This issue is discussed in more detail in the following section.

We want to further address the question of whether the seemingly improved nanorod growth in T45 could result from the remarkably lower thickness of the associated film when compared with the other samples. This is not the case because the $J_c$ values of BZO-doped YBCO films have shown to remain approximately constant as a function of the film thickness in the range associated with this work.[43] Moreover, the BF-STEM images of T25 and T35 clearly show distorted nanorods already below 100 nm thickness (T45), suggesting a major difference in the assembly process of the nanorods between the samples. These remarks support our conclusion that the longer deposition distance indeed improves the nanorod growth despite the observed differences in the film thickness.

**Increased *c*-Axis Peak and Flux Pinning at High Fields.** Here, we concentrate on the difference between samples T35 and T45 because the growth of the nanorods is greatly disturbed in sample T25, and thus this deposition distance is obviously too short for depositing good-quality films for various applications. On the basis of the STEM results collected in Table 1, we can conclude that when increasing the deposition distance from 35 to 45 mm, the average nanorod diameter is decreased from 5.9 to 4.6 nm and their length is increased drastically from 27% to 81% of the total thickness of the film. In addition, the volume ratio of the nanorods is decreased with increasing deposition distance, leading to the fact that the volume of the nanorods from the whole volume is decreased from 50% to 33%. The effect of the nanorod diameter and especially its length and density are summarized in Figure 5d, where the *c*-axis peak is clearly increased in sample T45, especially up to a field of 6 T, being roughly equal


https://doi.org/10.1021/acsanm.2c04054
ACS Appl. Nano Mater. 2022, 5, 18159−18167

to the magnetic matching field determined from the estimated nanorod densities from the TEM images. This means that the APC nanorod growth and thus the flux pinning properties along the YBCO $c$ axis are unambiguously improved when the film growth mechanism is slower and the particle density in the laser plume is lower, as realized at a higher deposition distance than is usually optimized for the crystallographically optimal YBCO. Therefore, we can conclude that the deposition process for improving the plateau area of the $J_c(B)$ curve should be different in comparison with the optimization of the flux pinning mechanism in the high-field range.

In order to study whether the improved $J_c$ can be attributed to the increased pinning performance of the thinner but more elongated nanorods of T45 compared with T35, we simulated the vortex-dynamics-limited $J_c(\theta)$ for pinning structures, mimicking the observations of the BF-STEM images for the corresponding samples presented in Figure 3. The applied simulation is a MD-based model that is briefly introduced in Figure S2, while a detailed description and extensive validation is presented in the Supporting Information in ref 44. The simulations were conducted using a 150 × 150 × 40 nm$^3$ sized grid, with a total of 21 distinct vortices. A single vortex was modeled as a chain of 10 adjacent particles (Figure S2). The pinning structure for T35 was modeled as randomly positioned stacks of three adjacent pinning site particles separated by a distance of 4.5 nm along the $c$ axis of YBCO. The nanorods were assigned with a radius ($R$ = 2.95 nm) corresponding to the results obtained from the BF-STEM images. The total number of aforementioned nanorods ($N$) was calculated using the observed average nanorod separation ($\overline{s}$ = 6 nm), resulting in $N = A/(R + \overline{s})^2 = 280$. Correspondingly, the pinning structure for T45 was modeled using stacks of eight pinning site particles with $R$ = 2.3 nm and $\overline{s}$ = 9 nm, resulting in $N$ = 176. The pinning structures for both T35 and T45 are schematically illustrated in Figure S3.

The simulated $J_c(\theta)$ curves for T35 and T45 are presented in the main panel of Figure 6. The simulations are in good agreement with the experimental observations presented in Figure 5 because the $c$ peak cannot be observed for T35, while it clearly emerges for T45 as the field is increased. The difference between the simulated anisotropy curves for T45 and T35 is further illustrated in the inset of Figure 6, which clearly resembles the corresponding experimental observations presented in Figure 5d. Thus, we conclude that the experimentally observed increased pinning performance of T45 results from better elongation of the BZO nanorods despite the decreased radius.

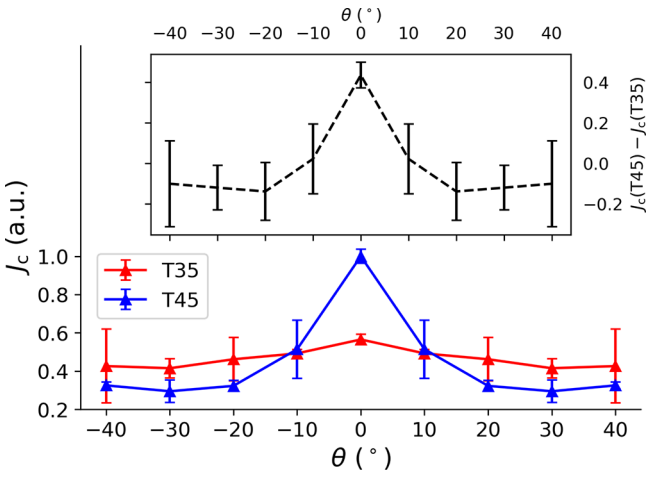


**Figure 6.** Simulated vortex-dynamics-limited $J_c(\theta)$ for T35 and T45, respectively, normalized by the maximum $J_c$ obtained for T45. The values of the data points represent the average of three statistical repeats, while the error bars correspond to the associated standard deviation. Inset: Difference between the simulated $J_c(\theta)$ curves for T45 and T35 presented in the main panel to make a better comparison with the experimental results shown in Figure 5d.

**Improved BZO Nanorod Growth as a Function of the Deposition Distance.** We have done an extensive review of literature related to the PLD process in order to explain why increasing the deposition distance improves the nanorod growth. To our knowledge, no rigorous experiments of theoretical study exist that would directly address this issue. However, applying several generally accepted ideas and theories related to different stages of the PLD process, we have managed to generate a semiquantitative model that reliably explains the observed results.

As a first approximation, we consider only single atoms, or ions, that are ablated from the target material and reach the substrate without being part of any chemical reactions in between. The probability that such an ablated atom gets attached to the top of the preexisting cluster on the surface of the substrate is governed by the associated Gibbs free energy ($G$), which tends to be minimized under constant pressure and temperature.[1] The Gibbs free energy has the pressure dependence[1,45]

$$G(P) = -kT \ln\left(\frac{P}{P_0}\right) \tag{2}$$

where $P$ is the partial pressure associated with the ablated atoms and $P_0$ is the constant vapor pressure of the cluster. $G$ decreases as a function of $P$, meaning that the probability that a particle attaches to a specific cluster increases when the partial pressure for that specific atomic species is increased.

We will generalize the above conclusions to the formation of unit cells on the substrate. We consider two different processes relevant to the formation of nanorods illustrated in Figure 7. The first process is the formation of a BZO unit cell on top of the preexisting BZO cluster on the surface of the substrate. It is intuitive to assume that the probability of this event is correlated with the partial pressure of the ablated Zr atoms

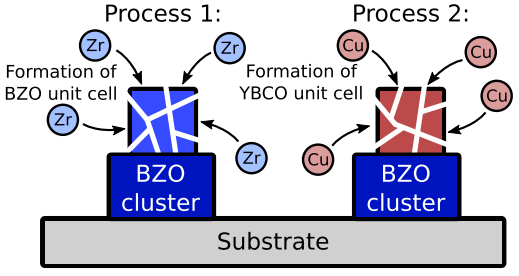


**Figure 7.** Schematic illustration of the two considered processes governing the formation of nanorods. In process 1, a BZO unit cell forms on top of the existing BZO cluster located on the surface of the substrate. The probability of this process correlates with the partial pressure of the ablated Zr atoms. In process 2, a YBCO unit cell forms on top of the existing BZO cluster. The associated probability correlates with the partial pressure of the ablated Cu atoms in the vicinity of the substrate.



https://doi.org/10.1021/acsanm.2c04054
ACS Appl. Nano Mater. 2022, 5, 18159−18167

($P_{Zr}$) in the vicinity of the substrate because Zr is the lightest metal element in the BZO unit cell and is not present in YBCO. The other considered process is the formation of a YBCO unit cell on top of the BZO cluster, which, in turn, is correlated to the partial pressure of the ablated Cu atoms ($P_{Cu}$), where Cu is the lightest element within YBCO and absent in BZO. The ratio between the probabilities of the above-mentioned processes is what ultimately decides the quality of the nanorods formed. That is, increasing the probability for the formation of YBCO on top of the BZO cluster intuitively results in poor-quality fragmented nanorods, while decreasing the associated probability will lead to the desired well-elongated nanorods. In summary, one ultimately has to address the ratio $P_{Zr}/P_{Cu}$ in the vicinity of the substrate in order to study nanorod formation as a function of the deposition distance.

We address the deposition distance dependence of $P_{Zr}/P_{Cu}$ by assuming that the dynamics of the ablated atoms is governed by the Langevin equation[46]

$$m\dot{\mathbf{v}} = -\gamma\mathbf{v} + \mathbf{R}(t) \tag{3}$$

where $\gamma$ is the drag coefficient and $\mathbf{R}(t)$ is a Gaussian random force associated with zero mean resulting from interaction of the particle with the background gas. The expectation value of the velocity as a function of time can be solved from eq 3 by neglecting $\mathbf{R}(t)$ and solving the resulting homogeneous differential equation. Assuming that all of the ablated particles obtain the same kinetic energy ($E$) from the laser−target interaction corresponding to the initial velocity $v(t{=}0) = \sqrt{2E/m}$ along the direction of the ablation axis, one obtains

$$\langle v(t)\rangle = \sqrt{\frac{2E}{m}}\, e^{-\gamma t/m} \tag{4}$$

This suggests that the velocities of the ablated particles decay exponentially, the rate of which is substantially higher for lighter elements. This further justifies the previously declared assumption that formation the BZO and YBCO unit cells is mainly correlated with the partial pressure of the ablated Zr ($m_{Zr}$ = 91.2 u) and Cu ($m_{Cu}$ = 63.5 u) atoms because they are the lightest elements within the associated unit cells and thus their partial pressures are most substantially limited for large deposition distances.

When the ablated Zr and Cu atoms are modeled as an ideal gas, the relative partial pressure between Zr and Cu can be expressed in terms of momentum as[45]

$$\frac{P_{Zr}}{P_{Cu}} = \frac{m_{Zr}\langle v_{Zr}(t)\rangle}{m_{Cu}\langle v_{Cu}(t)\rangle} \tag{5}$$

where the expected velocities are expressed by eq 4. Written open, one obtains

$$\frac{P_{Zr}}{P_{Cu}} = \sqrt{\frac{m_{Zr}}{m_{Cu}}}\, e^{-\gamma t(1/m_{Zr} - 1/m_{Cu})} \tag{6}$$

where $t$ can be interpreted as the time it takes for the ablated atom to travel from the target to the substrate. Thus, the time dependence of $P_{Zr}/P_{Cu}$ expressed by eq 6 also corresponds to the associated dependence on the deposition distance. Because $m_{Zr} > m_{Cu}$, the exponent in eq 6 is positive, and thus the relative pressure $P_{Zr}/P_{Cu}$ increases as a function of the deposition distance. This results in an increasing probability of BZO clusters being accompanied by BZO unit cells instead of YBCO as the target−substrate distance is increased, manifesting as the experimentally observed improved growth of a BZO nanorod for larger deposition distances. This also explains the decreased nanorod density with increasing deposition distance, as observed by STEM.

## CONCLUSIONS

In this work, the effect of the deposition distance on the film thickness, crystalline quality, superconducting properties, and especially flux pinning in BZO-doped YBCO thin films is systematically studied. On the basis of structural analysis, as expected, the earlier optimized and hardware-specific deposition distance produced the best crystalline quality and thus also the highest critical temperature. However, although the concentration of the elements in films deposited at different distances stays the same, defect formation in the YBCO lattice and especially the growth mechanism of the self-assembled BZO nanorods are greatly modified, totally affecting the flux pinning characteristic and thus significantly improving the critical current densities at higher deposition distances.

According to STEM analysis, at higher deposition distances, the BZO nanorods are smaller in diameter, they are better aligned along the YBCO $c$ axis, and their density is smaller, but the foremost result is that the nanorods are relatively so much longer that they are grown almost through the entire film. This is only the case at the highest deposition distance, naturally affecting the anisotropy of the critical current by forming a clearly pronounced $c$-axis peak in the $J_c(\theta)$ curve, especially at high magnetic fields. The formation of lengthened BZO nanorods is also confirmed by MD simulations, where, regardless of the decreased nanorod density, the straight and long nanorods produce a relatively narrow but significantly higher $c$-axis peak. In order to understand the mechanisms behind the improved nanorod growth for larger deposition distances, we created a semiquantitative model that explains the experimentally observed features through variation of the fractional partial pressure between atomic species within the laser plume as a function of the distance from the substrate. We have concluded that this variation results in a higher probability of BZO unit cells stacking on top of each other as the target−substrate distance is increased. On this basis, we can conclude that tuning the deposition distance can be a notable tool for manipulating the growth of APCs also in other thin-film or coated conductor systems, which again may have a major significance in future HTS power application technologies.

## ASSOCIATED CONTENT

### Supporting Information

The Supporting Information is available free of charge at https://pubs.acs.org/doi/10.1021/acsanm.2c04054.

Structural properties from XRD measurements, X-ray 2$\theta$ diffractograms, schematic illustration of the utilized MD-based simulation model, and 3-dimensional schematic illustration of the pinning structures used in the simulations for T35 and T45 (PDF)

## AUTHOR INFORMATION

### Corresponding Authors

**Moe Moe Aye** − *Wihuri Physical Laboratory, Department of Physics and Astronomy, University of Turku, 20014 Turku,*



https://doi.org/10.1021/acsanm.2c04054
ACS Appl. Nano Mater. 2022, 5, 18159−18167

*Finland; University of Turku Graduate School, University of Turku, 20014 Turku, Finland;* orcid.org/0000-0001-8021-118X; Email: moe.m.aye@utu.fi

**Elmeri Rivasto** − *Wihuri Physical Laboratory, Department of Physics and Astronomy, University of Turku, 20014 Turku, Finland; University of Turku Graduate School, University of Turku, 20014 Turku, Finland;* orcid.org/0000-0002-1255-0726; Email: elmeri.o.rivasto@utu.fi

## Authors

**Hannes Rijckaert** − *SCRiPTS, Department of Chemistry, Ghent University, 9000 Ghent, Belgium;* orcid.org/0000-0002-6078-2919

**Sari Granroth** − *Materials Research Laboratory, Department of Physics and Astronomy, University of Turku, FI-20014 Turku, Finland*

**Heikki Palonen** − *Wihuri Physical Laboratory, Department of Physics and Astronomy, University of Turku, 20014 Turku, Finland*

**Hannu Huhtinen** − *Wihuri Physical Laboratory, Department of Physics and Astronomy, University of Turku, 20014 Turku, Finland*

**Isabel Van Driessche** − *SCRiPTS, Department of Chemistry, Ghent University, 9000 Ghent, Belgium;* orcid.org/0000-0001-5253-3325

**Petriina Paturi** − *Wihuri Physical Laboratory, Department of Physics and Astronomy, University of Turku, 20014 Turku, Finland*

Complete contact information is available at: https://pubs.acs.org/10.1021/acsanm.2c04054

## Notes

The authors declare no competing financial interest.

## ■ ACKNOWLEDGMENTS

The Jenny and Antti Wihuri Foundation and the University of Turku Graduate School are acknowledged for financial support. H.R. gratefully acknowledges support and funding as postdoctoral fellow fundamental research of the Research Foundation—Flanders under Grant 1273621N. The computer resources of the Finnish IT Center for Science and the FGCI project (Finland) are acknowledged.

## ■ REFERENCES

(1) Chrisey, D. B.; Hubler, G. K.*Pulsed Laser Deposition of Thin Films*; John Wiley Sons Inc., 1994.

(2) Dijkkamp, D.; Venkatesan, T.; Wu, X. D.; Shaheen, S. A.; Jisrawi, N.; Min-Lee, Y. H.; McLean, W. L.; Croft, M. Preparation of Y-Ba-Cu oxide superconductor thin films using pulsed laser evaporation from high $T_c$ bulk material. *Appl. Phys. Lett.* **1987**, *51*, 619.

(3) Venkatesan, T.; Wu, X. D.; Inam, A.; Jeon, Y.; Croft, M.; Chase, E. W.; Chang, C. C.; Wachtman, J. B.; Odom, R. W.; di Brozolo, F. R.; Magee, C. A. Nature of the pulsed laser process for the deposition of high $T_c$ superconducting thin films. *Appl. Phys. Lett.* **1988**, *53*, 1431.

(4) Foltyn, S. R.; Civale, L.; MacManus-Driscoll, J. L.; Jia, Q. X.; Maiorov, B.; Wang, H.; Maley, M. Materials science challenges for high-temperature superconducting wire. *Nat. Mater.* **2007**, *6*, 631−642.

(5) Maiorov, B.; Baily, S. A.; Zhou, H.; Ugurlu, O.; Kennison, J. A.; Dowden, P. C.; Holesinger, T. G.; Foltyn, S. R.; Civale, L. Synergetic combination of different types of defect to optimize pinning landscape using $BaZrO_3$-doped $YBa_2Cu_3O_7$. *Nat. Mater.* **2009**, *8*, 398−404.

(6) Malmivirta, M.; Yao, L.; Huhtinen, H.; Palonen, H.; van Dijken, S.; Paturi, P. Three ranges of the angular dependence of cirtical current of $BaZrO_3$ doped $YBa_2Cu_3O_{7-\delta}$ thin films grown at different temperatures. *Thin Solid Films* **2014**, *562*, 554−560.

(7) Rivasto, E.; Khan, M. Z.; Wu, Y.; Zhao, Y.; Chen, C.; Zhu, J.; Huhtinen, H.; Paturi, P. Lattice defect induced nanorod growth in YBCO films deposited on an advanced IBAD-MgO template. *Supercond. Sci. Technol.* **2020**, *33*, 075008.

(8) Traito, K.; Peurla, M.; Huhtinen, H.; Stepanov, Y. P.; Safonchik, M.; Tse, Y. Y.; Paturi, P.; Laiho, R. Magnetic field dependence of the critical current and the flux pinning mechanism in $YBa_2Cu_3O_{6+x}$ films doped with $BaZrO_3$. *Phys. Rev. B* **2006**, *73*, 224522.

(9) Wu, J. Z.; Shi, J. J.; Baca, F. J.; Emergo, R.; Wilt, J.; Haugan, T. J. Controlling $BaZrO_3$ nanostructure orientation in $YBa_2Cu_3O_{7-\delta}$ films for a three-dimensional pinning landscape. *Supercond. Sci. Technol.* **2015**, *28*, 125009.

(10) Wu, J.; Shi, J. Interactive modeling-synthesis-characterization approach towards controllable in situ self-assembly of artificial pinning centers in RE-123 films. *Supercond. Sci. Technol.* **2017**, *30*, 103002.

(11) Aye, M. M.; Rivasto, E.; Khan, M. Z.; Rijckaert, H.; Palonen, H.; Huhtinen, H.; Van Driessche, I.; Paturi, P. Multilayering BZO nanocolumns with different defect densities for YBCO high field applications. *New J. Phys.* **2021**, *23*, 113031.

(12) Paturi, P.; Huhtinen, H. Roles of electron mean free path and flux pinning in optimizing the critical current in YBCO superconductors. *Supercond. Sci. Technol.* **2022**, *35*, 065007.

(13) Khan, M. Z.; Rivasto, E.; Tikkanen, J.; Rijckaert, H.; Malmivirta, M.; Liedke, M. O.; Butterling, M.; Wagner, A.; Huhtinen, H.; Van Driessche, I.; Paturi, P. Enhanced flux pinning isotropy by tuned nanosized defect network in superconducting $YBa_2Cu_3O_{6+x}$ films. *Sci. Rep.* **2019**, *9*, 15425.

(14) Rivasto, E.; Khan, M. Z.; Malmivirta, M.; Rijckaert, H.; Aye, M. M.; Hynninen, T.; Huhtinen, H.; Driessche, I. V.; Paturi, P. Self-assembled nanorods in YBCO matrix − a computational study of their effects on critical current anisotropy. *Sci. Reports* **2020**, *10*, 3169.

(15) Huhtinen, H.; Paturi, P.; Lähderanta, E.; Laiho, R. Laser deposition of thin superconducting films from a nanocrystalline YBCO target. *Supercond. Sci. Technol.* **1999**, *12*, 81−86.

(16) Huhtinen, H.; Järvinen, J.; Laiho, R.; Paturi, P.; Raittila, J. Laser deposition from a nanostructured YBaCuO target: Analysis of the plume and growth kinetics of particles on $SrTiO_3$. *J. Appl. Phys.* **2001**, *90*, 1521−1528.

(17) Dyer, P. E.; Issa, A.; Key, P. H. Dynamicks of excimer laser ablation of superconductors in an oxygen environment. *Appl. Phys. Lett.* **1990**, *57*, 186.

(18) Kumuduni, W. K. A.; Nakata, Y.; Sasaki, Y.; Okada, T.; Maeda, M.; Kisu, T.; Takeo, M.; Enpuku, K. Effect of cumulative ablation on the ejection of particulates and molecular species from $YBa_2Cu_3O_{7-x}$ targets. *J. Appl. Phys.* **1995**, *77*, 5961.

(19) Garrelie, E.; Champeaux, C.; Catherinot, A. Expansion dynamics of the plasma plume created by laser ablation in a background gas. *Appl. Phys. A: Mater. Sci. Process.* **1999**, *69*, S55.

(20) Pysarenko, S. V.; Pan, A. V.; Dou, S. X. Origin of surface morphology variation during pulsed laser deposition of YBCO superconducting films. *IEEE T. Appl. Supercond.* **2011**, *21*, 3179.

(21) Golovchanskiy, I. A.; Pan, A. V.; Fedoseev, S. A.; Higgins, M. Significant tunability of thin film functionalities enabled by manipulating magnetic and structural nano-domains. *Appl. Surf. Sci.* **2014**, *311*, 549−557.

(22) Rao, C. N. R.; Nagarajan, R.; Vijayaraghaven, R. Synthesis of cuprate superconductors. *Supercond. Sci. Technol.* **1993**, *6*, 1−22.

(23) Palonen, H.; Huhtinen, H.; Shakhov, M. A.; Paturi, P. Electron mass anisotropy of $BaZrO_3$ doped YBCO thin films in pulsed magnetic fields up to 30 T. *Supercond. Sci. Technol.* **2013**, *26*, 045003.

(24) Rijckaert, H.; Pollefeyt, G.; Sieger, M.; Hänisch, J.; Bennewitz, J.; De Keukeleere, K.; De Roo, J.; Hühne, R.; Bäcker, M.; Paturi, P.; Huhtinen, H.; Hemgesberg, M.; Van Driessche, I. Optimizing Nanocomposites through Nanocrystal Surface Chemistry: Superconducting YBCO Thin Films via Low Fluorine Metal Organic Deposition and Preformed Metal Oxide Nanocrystals. *Chem. Mater.* **2017**, *29*, 6104−6113.

(25) Wiesinger, H. P.; Sauerzopf, F. M.; Weber, H. W. On the calculation of $J_c$ from magnetization measurements on superconductors. *Physica C* **1992**, *203*, 121−128.
(26) Larbalestier, D.; Gurevich, A.; Feldmann, D. M.; Polyanskii, A. High-$T_c$ superconducting materials for electric power applications. *Nature* **2001**, *414*, 368−377.
(27) Paturi, P.; Malmivirta, M.; Hynninen, T.; Huhtinen, H. Angle dependent molecular dynamics simulation of flux pinning in YBCO superconductors with artificial pinning sites. *J. Phys. Cond. Mater.* **2018**, *30*, 315902.
(28) Rivasto, E.; Huhtinen, H.; Hynninen, T.; Paturi, P. Vortex dynamics simulation for pinning structure optimization in the applications of high- temperature superconductors. *J. Phys. Cond. Mater.* **2022**, *34*, 235902.
(29) Ye, J.; Nakamura, K. Quantitative structure analyses of YBCO thin films: Determination of oxygen content from x-ray-diffraction patterns. *Phys. Rev. B* **1993**, *48*, 7554−7564.
(30) Als-Nielsen, J.; McMorrow, D.*Elements of Modern X-ray Physics*; Wiley, 2010.
(31) Aye, M. M.; Khan, M. Z.; Rivasto, E.; Tikkanen, J.; Huhtinen, H.; Paturi, P. Role of Columnar Defect Size in Angular Dependent Flux Pinning Properties of YBCO Thin Films. *IEEE T. Appl. Supercond.* **2019**, *29*, 1.
(32) Peurla, M.; Huhtinen, H.; Shakhov, M. A.; Traito, K.; Stepanov, Y. P.; Safonchik, M.; Paturi, P.; Tse, Y. Y.; Palai, R.; Laiho, R. Effects of nanocrystalline target and columnar defects on flux pinning in pure and BZO-doped YBCO films in fields up to 30 T. *Phys. Rev. B* **2007**, *75*, 184524.
(33) Cantoni, C.; Gao, Y.; Wee, S. H.; Specht, E. D.; Gazquez, J.; Meng, J.; Pennycook, S. J.; Goyal, A. Strain-driven oxygen deficiency in self-assembled, nanostructured, composite oxide films. *ACS Nano* **2011**, *5*, 4783−4789.
(34) Majkic, G.; Jeong, J. S.; Yun, H.; Robles Hernandez, F. C.; Galstyan, E.; Pratap, R.; Cheng, H.; Stokes, A.; Mkhoyan, K. A.; Selvamanickam, V. New insight into strain and composition of $BaZrO_3$ nanorods in REBCO superconductor. *Supercond. Sci. Technol.* **2021**, *34*, 115002.
(35) Qin, M. J.; Shi, Z. X.; Ji, H. L.; Jin, X.; Yao, X. X.; Li, H. C.; Rong, X. S. Paramagnetism and scaling behavior of volume flux pinning force density in a $GdBa_2Cu_30_{6+x}$ thin films. *J. Appl. Phys.* **1995**, *78*, 3287.
(36) Varanasi, C. V.; Barnes, P. N.; Burke, J. Enhanced flux pinning force and uniquely shaped flux pinning force plots observed in $YBa_2Cu_3O_{7-x}$ films with $BaSnO_3$ nanoparticles. *Supercond. Sci. Technol.* **2007**, *20*, 1071.
(37) Paturi, P.; Malmivirta, M.; Palonen, H.; Huhtinen, H. Dopant Diameter Dependence of $J_c(B)$ in Doped YBCO Films. *IEEE T. Appl. Supercond.* **2016**, *26*, 1.
(38) Long, N. J. Model for the angular dependence of critical currents in technical superconductors. *Supercond. Sci. Technol.* **2008**, *21*, 025007.
(39) Wimbush, S.; Long, N. The interpretation of the field angle dependence of the critical current in defect-engineered superconductors. *New J. Phys.* **2012**, *14*, 083017.
(40) Sueyoshi, T. Modification od critical current density anisotropy in high-$T_c$ superconductors by using heavy-ion irradiations. *Quantum Beam Sci.* **2021**, *5*, 16.
(41) Matsushita, T.; Isobe, G.; Kimura, K.; Kiuchi, M.; Okayasu, S.; Prusseit, W. The effect of heavy ion irradiation on the critical current density in DyBCO coated conductors. *Supercond. Sci. Technol.* **2008**, *21*, 054014.
(42) Strickland, N.; Talantsev, E.; Long, N.; Xia, J.; Searle, S.; Kennedy, J.; Markwitz, A.; Rupich, M.; Li, X.; Sathyamurthy, S. Flux pinning by discontinuous columnar defects in 74 MeV Ag-irradiated $YBa_2$ $Cu_3$ $O_7$ coated conductors. *Physica C* **2009**, *469*, 2060−2067.
(43) Wang, X.; Baca, F. J.; Emergo, R. L. S.; Wu, J. Z.; Haugan, T. J.; Barnes, P. N. Eliminating thickness dependence of critical current density in $YBa_2Cu_3O_{7-x}$ films with aligned $BaZrO_3$ nanorods. *J. Appl. Phys.* **2010**, *108*, 113911.
(44) Rivasto, E.; Hynninen, T.; Huhtinen, H.; Paturi, P.Optimization of high-temperature superconducting bilayer structures using a vortex dynamics simulation. *J. Phys. Cond. Mater.***2022**, DOI: 10.1088/1361-648X/ac9f97
(45) Schroeder, D.*An Introduction to Thermal Physics*; Oxford University Press, 2000.
(46) Coffey, W.; Kalmykov, Y. P.*The Langevin Equation: With Applications to Stochastic Problems in Physics, Chemistry and Electrical Engineering*; World Scientific, 2012.